Journal of Power Sources 630 (2025) 236144

Contents lists available at ScienceDirect

Journal of Power Sources

journal homepage: www.elsevier.com/locate/jpowsour

Plasma induced oxygen vacancies on high entropy oxide surfaces for efficient overall water splitting

Amarnath Pasupathi [a], Ragunath Madhu [b,c], Subrata Kundu [c,**], Yugeswaran Subramaniam [a,*]

[a] Applied Thermal Plasma Laboratory, Department of Physics, Pondicherry University, Puducherry, 605014, India
[b] Academy of Scientific and Innovative Research (AcSIR), Ghaziabad, 201002, India
[c] Electrochemical Process Engineering (EPE) Division, CSIR-Central Electrochemical Research Institute (CECRI), Karaikudi, 630003, Tamil Nadu, India

HIGHLIGHTS

- Non-thermal plasma is a promising tool for creating oxygen vacancies on HEO surfaces.
- The creation of oxygen vacancies enhances the OER and HER performance of HEO.
- HEO requires overpotential of 246 mV (OER) and 197 mV (HER) to reach 50 mA cm^{-2}
- HEO needs 1.58V for overall water splitting to reach a current density of 10 mA cm^{-2}

GRAPHICAL ABSTRACT

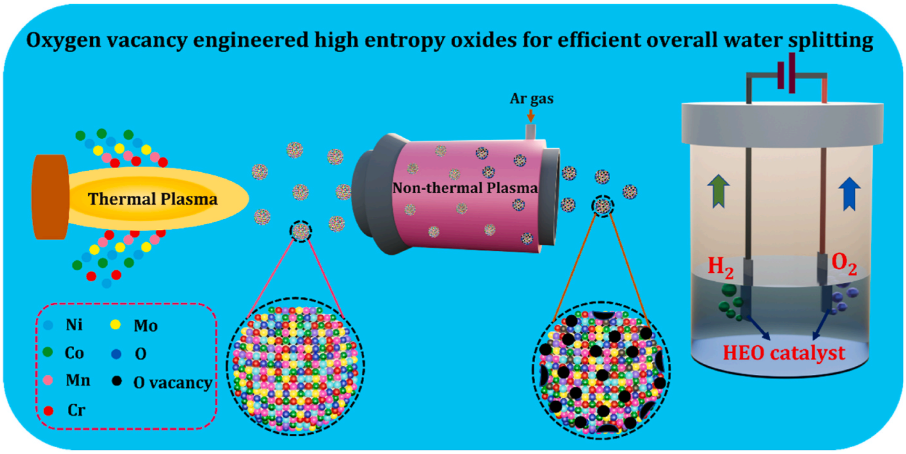

ARTICLE INFO

Keywords:
Oxygen vacancy
High entropy oxides
Thermal plasma technology
Electrocatalyst
Water splitting

ABSTRACT

Oxygen vacancy engineering emerges as a pioneering and effective approach for accelerating electrocatalytic activity in conventional metal oxide electrocatalysts and is recognized as a viable alternative to noble materials. In this study, a DC non-transferred arc thermal plasma torch is used to synthesize high entropy oxides (HEOs) (Ni, Co, Cr, Mn, Mo)$_3$O$_4$ nanoparticles under optimal operating conditions, and oxygen vacancies are created on the surface of the as-synthesized nanoparticles by treating them with Ar-glow discharge plasma. The oxygen vacancy-induced HEOs nanoparticles are characterized using various microscopic and spectroscopic techniques. The results reveal that increasing the Ar-plasma treatment time (0, 5, 10, 15 min) increases the surface oxygen vacancy. The electrochemical water-splitting performance of oxygen vacancy-induced HEOs nanoparticles is examined in 1 M KOH electrolyte solution employing them as an electrocatalyst. Oxygen vacancy rich HEOs nanoparticles demonstrate exceptional performance in both the oxygen evolution reaction (OER) and the hydrogen evolution reaction (HER), achieving an overpotential of 246 and 197 mV to achieve a current density

---

[*] Corresponding author.
[**] Corresponding author.

E-mail addresses: kundu@cecri.res.in (S. Kundu), yugeswaran@pondiuni.ac.in (Y. Subramaniam).

https://doi.org/10.1016/j.jpowsour.2024.236144
Received 23 November 2024; Received in revised form 27 December 2024; Accepted 28 December 2024

of 50 mA cm^{-2}. Eventually, a two-electrode device is fabricated, which requires a cell voltage of 1.58 V to achieve a current density of 10 mA cm^{-2}. This work pioneers a revolutionary technique for surface engineering in metal oxides nanoparticles using plasma technology, achieving exceptional performance in water splitting.

1. Introduction

Hydrogen energy economy has garnered unprecedented attention as a next-generation clean energy source, and it has been portrayed as a sustainable, environmentally friendly energy source capable of serving as a principal replacement for fossil fuels [1]. Hydrogen can be produced in a variety of methods, including dry reforming of methane [2], partial oxidation of methane [3], stream reforming of methane [4], and electrochemical water splitting [5]. Among these, electrochemical water splitting is regarded as a potential approach for the production of clean and green hydrogen from aqueous solutions without emitting carbon dioxide. It is composed of two half reactions: an oxygen evolution reaction (OER) at the anode and a hydrogen evolution reaction (HER) at the cathode, respectively [6]. Thermodynamically, 1.23 V potential is required to break the water molecules; but, in practice a high potential of 1.8 V was required to overcome the reaction activation barrier. Platinum (Pt), Iridium (Ir), and Ruthenium (Ru)-based catalysts were known to be “state-of-art” catalyst that reduce overpotential and accelerate the kinetics of HER and OER for effective water splitting [7]. However, there are significant limitations to the practical implementation of these catalysts, due to its high cost and scarcity on earth. Hence, the development of high-performance, long-lasting, and low cost electrocatalysts is crucial for effective water splitting [8]. Consequently, a transition metals with partially filled d-orbitals, such as molybdenum (Mo), tungsten (W), titanium (Ti), tantalam (Ta) and niobium (Nb) have enhanced catalytic activity because their M−H bond strengths fall within the optimal range indicated by the volcano plot. Their electronic configurations allow for efficient interaction with hydrogen, promoting better catalytic performance [9].

Sadhanala et al. [10] synthesized RuO_2 nanoparticles supported by MoO_3 nanosheets using a sonochemical method and evaluated their efficacy for water splitting. The material exhibited an outstanding exchange current density of 0.57 mA cm^{-2} and achieved a low overpotential of 110 mV at a current density of 10 mA cm^{-2} for the hydrogen evolution reaction in a 0.5 M H_2SO_4 electrolyte. A multi-metal oxide modified by their electronic structure and defects outperform single and binary metal oxides in water splitting performance due to the synergistic effects of multiple metal species, increased active sites, and enhanced charge transfer processes. These factors collectively contribute to the superior catalytic activity of multi-metal oxides [11].

Recently, a new class of multi-metal oxides, so-called high entropy oxides (HEOs), consists of five or more principal metal cations with an equal or near equal molar concentration combined to form a single-phase crystal structure, which has attracted attention due to their exceptional structural characteristics and excellent properties [12]. So far, numerous types of HEOs have been investigated and have demonstrated promising performance in electrocatalysis, including water splitting [7], oxygen reduction [13], and supercapacitor [12]. So far, wide range of synthesis methods have been adapted for the synthesis of HEOs nanoparticles, including solid state reaction [14], hydrothermal [15], co-precipitation [16], and solvothermal method [17]. However, the synthesis techniques utilized to produce HEO electrocatalysts can be exceedingly difficult, requiring multiple steps as well as severe pressure and temperature limitations. To address these issues, it is imperative to develop modern technology for the production of HEOs nanoparticles with high yield and cost-effective catalytic materials.

Recently, our group demonstrated that thermal plasma is a promising medium for synthesizing phase-pure HEOs nanoparticles in a single-step procedure. Plasma technology has been recognized as a novel and versatile technique for producing large quantities of pure nanoparticles [18]. This single-step process involves systematic evaporation, nucleation, and condensation. Thermal plasma has a high quenching rate, which promotes homogeneous nucleation and the formation of nanoparticles [19].

Numerous studies thoroughly investigate the remarkable water-splitting properties of various types of HEOs [16,20]. However, the influence of defect engineering, such as oxygen vacancy, dislocations, and stacking faults, on the as-synthesized HEO's water-splitting activity has yet to be thoroughly investigated. Oxygen vacancy engineering is a viable strategy for tuning the electronic structure of an electrocatalyst, surface adsorption/desorption of reactants, and increasing the electrical conductivity and charge transfer rate of materials. Oxygen vacancy is a type of point defect caused by the removal of an oxygen atom from a metal oxide lattice without facilitating a phase transformation. Different approaches can be used to create oxygen vacancies in metal oxides during synthesis or after synthesis, such as thermal treatment [21], reduction process [22], laser treatment [23], flame treatment [24], and plasma treatment [25]. Among them, plasma treatment is regarded as a powerful technique for the creation of oxygen vacancies, which shows good selectivity, high efficiency, relatively shorter treatment time (usually few minutes), chemical-free and environment friendly. Plasma treatment can be performed under various atmospheric conditions (Ar, O_2, N_2, NH_3, etc.) to produce oxygen vacancies and heteroatoms. Ding et al. [25] used Ar plasma to produce oxygen vacancies on HEOs (Fe, Ni, Co, Mn, V)O nanoparticles which synthesized using the solvothermal method and studied their HER performance. The findings demonstrate that plasma-treated sample exhibits superior HER performance compared to their as-synthesized counterparts.

In this study, thermal plasma technology was employed to synthesize HEOs $(Ni, Co, Cr, Mn, Mo)_3O_4$ nanoparticles under optimized processing conditions. Subsequently, surface oxygen vacancies were created on the synthesized HEOs nanoparticles by subjecting them to argon glow discharge plasma. The glow discharge plasma was generated under conditions of 3 Pa pressure and 400 V, facilitating the bombardment of energetic Ar ions onto the nanoparticle surfaces to remove oxygen atoms from the metal surface. The influence of glow discharge plasma treatment time on the formation of surface oxygen vacancies, as well as the simultaneous effect on the oxygen and hydrogen evolution reactions, was systematically investigated.

2. Materials and methods

2.1. Materials

All the chemicals utilized in this work are analytical grade and were used without further purification. Chromium (III) nitrate nanohydrate ($Cr(NO_3)_3.9H_2O$, Sigma Aldrich), cobalt (II) nitrate hexahydrate ($Co(NO_3)_2.6H_2O$, Sigma Aldrich), manganese (II) nitrate ($Mn(NO_3)_2.xH_2O$, Sigma Aldrich), nickel (II) nitrate hexahydrate [$Ni(NO_3)_2{\cdot}6H_2O$, Sigma Aldrich], and molybdenum (V) chloride ($MoCl_5$, Sigma Aldrich) were purchased.

2.2. Experimental setup

The HEOs nanoparticles were synthesized by using DC thermal plasma reactor in vapour phase condensation technique. The experimental setup, plasma torch and plasma jet characterization were comprehensively described in our previous studies [18,26,27]. All the constituent precursor materials (Ni, Co, Cr, Mn and Mo) were taken in equimolar concentration and dissolved in 30 ml double distilled water.

After homogenous mixing of all the precursor solution, the mixture was atomized and injected into the thermal plasma jet through the liquid feeder which was positioned perpendicular to the plasma torch approximately 20 mm below the nozzle exit. Table 1 depicts the typical plasma torch operating parameters. Herein, Ar gas was used to ignite the pilot arc and a working gas CO_2 was gradually introduced into the plasma torch, it produces highly stable and high enthalpy plasma jet. The presence of highly reactive species, higher thermal conductivity, and high temperature environment, provokes the thermal decomposition and effectively evaporate the precursor material and forms as a metal vapour cloud. After attaining a supersaturation state of all the metal vapours, nucleation primarily begins, and subsequently condensed on the walls of the chamber. Deposited nanoparticles were carefully collected from the chamber and annealed at 100 °C for 4 h to remove the unwanted impurities and moisture present in the nanoparticles.

2.3. *Creation of oxygen vacancies*

The schematic representation of low-pressure glow discharge plasma used for the creation of oxygen vacancy on as-synthesized HEOs surface is shown in Fig. 1. A customized low-pressure glow discharge plasma reactor (Hydro Pneo Vac Technologies (HPVT), Bengaluru, India) made of a stainless-steel chamber (length: 0.3 m; width: 0.3 m) was used to generate glow discharge plasma. The as-synthesized powder sample (250 mg) to be treated was placed between the electrodes (cathode and anode) with the help of a sample holder made of Teflon, which had a thickness of 2 mm and a diameter of 9 mm. The chamber was evacuated using a rotary pump and flushed multiple times with argon gas to remove impurities. After establishing a base pressure of 3 Pa, a glow discharge was initiated with a high-voltage DC power source set to 400 V, using argon as the plasma gas. At a total discharge power of 120 W, HEOs nanoparticles were treated with plasma for different durations (i.e.) 5, 10, and 15 min. These samples were labelled as HEO O5, HEO O10, and HEO O15, respectively. The as-synthesized nanoparticles without plasma treatment were labelled as HEO O0.

2.4. *Material characterization*

The crystal structure and crystalline size was investigated by X-ray diffraction (XRD) using Rigaku Smartlab diffractometer with a Cu-kα radiation (1.54056 Å) at 30 mA current and 40 kV accelerated voltage. The XRD pattern was recorded from 15 to 65° with a scan rate of 10°/min. Morphology and elemental distribution of the HEOs nanoparticles was characterized by field emission scanning electron microscopy and energy dispersive X-ray spectrometer (FE-SEM-EDX; SIGMA HV-Carl Zeiss with Bruker Quantax 200 and Z10 EDX detector). The microstructural information was analysed by high resolution transmission electron microscopy (HR-TEM; Tecnai™ G2 TF20) with the selected area electron diffraction (SAED) pattern. The surface chemistry and oxidation state of HEOs nanoparticles was examined by X-ray photoelectron spectroscopy (XPS; Thermo Scientific, K-Alpha-KAN995413), using Al Kα radiation (1486.6 eV). The oxygen vacancy can be detected by the electron paramagnetic resonance spectroscopy (EPR; Bruker Biospin, EMX plus X Band). The UV–visible spectrophotometer (UV–Vis; Shimadzu, 3600) was used to record the diffused reflectance spectra of the HEO nanoparticles between 200 and 800 nm wavelength range.

Table 1
Plasma torch operating parameters.

Parameter	Value
Arc current (A)	75
Arc voltage (V)	147
Plasma power (kW)	~11
Plasma generating gas (Ar) flow rate (slpm)	15
Secondary working gas (CO_2) flow rate (slpm)	20

2.5. *Electrochemical measurements*

The electrochemical properties were measured using a Metrohm AUTOLAB-M240 instrument with techniques like CV, and chronopotentiometry. All the electrochemical experiments were carried out by employing a conventional three-electrode set-up. The working electrodes were fabricated using 1 mg of Polyvinylidene fluoride (PVDF) as a binder and N-Methyl-2-pyrrolidone (NMP) as a slurry preparation agent. Typically, the ≈4:1 (with respect to overall catalyst loading over the electrode surface) ratio of powder catalyst and PVDF had taken into a mortar, followed by the addition of NMP solvent with continuous mixing by a pestle. Then a certain amount of catalyst ink was fabricated over the 1 cm^2 area of the nickel foam (NF) [28]. The amount of loaded catalyst was calculated by measuring the difference in weight of coated and uncoated NF.

For OER and HER in 1 M KOH solution, the commercial Hg/HgO, and Pt-ring (for OER)/graphite (for HER) [29] were used as a reference and counter electrodes, respectively.

3. Results and discussion

3.1. *Physicochemical characterization*

Fig. 1 insert image shows the optical emission spectrum (OES) of low-pressure glow discharge Ar-plasma used to treat the as-synthesized HEOs nanoparticles. The spectrum reveals distinct Ar (2 pH - 1sG) emission lines in the wavelength range of 650–850 nm. The presence of energetic Ar ions and neutral species in the low-pressure glow discharge plasma results in continuous bombardment of the HEO nanoparticle surface. This bombardment transfers kinetic energy to the surface atoms, displacing oxygen atoms from the lattice sites and creating oxygen vacancies. The formation of oxygen vacancies is influenced by several factors, including plasma exposure time, pressure, and plasma power. Moreover, the interaction between the Ar species and the material surface generates localized heating, which increases the mobility of surface atoms. This enhanced mobility promotes the more efficient ejection of oxygen atoms from the HEO lattice sites. Consequently, the creation of oxygen vacancies is further amplified, leading to an increase in the number of surface-active sites. This process not only enhances charge transfer but also improves the adsorption-desorption kinetics, both of which are essential for improving the catalytic performance of HEO nanoparticles in reactions such as oxygen evolution and hydrogen evolution.

Fig. 2 shows the XRD pattern of as-synthesized and Ar-plasma treated HEOs nanoparticles with different treatment time. It shows that the seven diffraction peaks at 18.12°, 29.87°, 35.35°, 36.81°, 42.85°, 56.77°, and 62.67° correspond to the (111), (220), (311), (222), (400), (511), and (440) planes of the spinel (Fd3m) structure, which were well matched with the crystal facets of $MnCr_2O_4$ (ICDD card No: 01-075-1614). Absence of additional peaks, implying that the synthesized HEOs nanoparticles have a phase pure spinel structure. After Ar-plasma treatment, the XRD patterns of HEOs nanoparticles retain their characteristic peaks, indicating that the crystal structure remains stable. Meanwhile, the intensity of the XRD pattern reduced as plasma exposure time increases. The plasma treatment often results in surface etching, roughness and defects in the surface of the material, which leads to reduce the crystallinity and lowers the intensity of the XRD pattern [30]. The crystalline size was determined using the Debye-Scherrer formula, and it was ranged from 10 to 19 nm [31].

The surface morphology of the HEOs nanoparticles can be investigated by FE-SEM analysis. Fig. 3a shows the FE-SEM image of HEO O15 and Figure S1(a, c and e) shows the FE-SEM images of HEO O0, HEO O5 and HEO O10, respectively. It is observed from the FE-SEM images, all the particles are close to spherical in shape with agglomeration and few

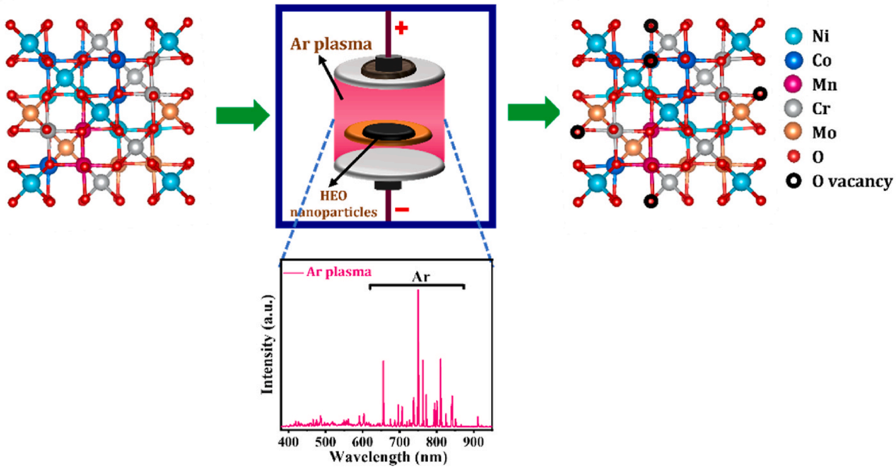

Fig. 1. Schematic representation of low-pressure glow discharge plasma for creation of oxygen vacancy on HEOs nanoparticles surface.

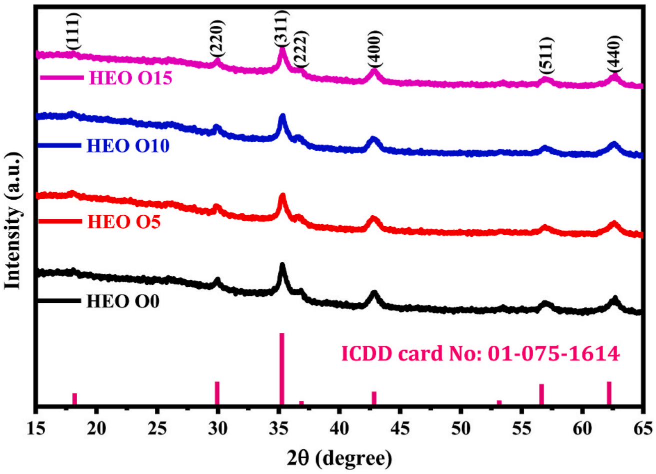

Fig. 2. XRD pattern of as-synthesized and Ar-plasma surface treated HEOs nanoparticles.

are quasi-spherical in nature [26]. Furthermore, the microstructural results reveals that the Ar-plasma treatment did not modify the surface morphology of the HEOs nanoparticles. EDX analysis was used to perform the elemental analysis of HEOs nanoparticles and shown in Fig. 3b and Figure S1(b, d and f). The acquired results confirm that all of the constituent elements (Ni, Mn, Mo, Cr, Co and O) are present in the HEOs nanoparticles, with larger oxygen atomic weight percentage than other elements based on spinel structure. It is observed that the oxygen content of the HEOs nanoparticles decreases as the plasma exposure time increases, implying an increase in oxygen vacancies with respect to Ar-plasma exposure time. According to the EDX results, oxygen vacancies on the surface of the HEOs nanoparticles were identified in the following order: HEO O15 > HEO O10 > HEO O5 > HEO O0. To further understand the elemental distribution of HEOs nanoparticles, elemental mapping was performed and displayed in Fig. 3c-h. The elemental mapping observation reveals that all of the elements were uniformly disturbed in the HEOs nanoparticles. Based on the percentage of each element's atomic weight, the elemental composition that was determined as $(Mo_{0.23}Cr_{0.22}Ni_{0.20}Mn_{0.18}Co_{0.17})_3O_4$. High entropy materials typically exhibit a configurational entropy greater than 1.5R. For the as-synthesized HEOs, the actual configurational entropy was determined to be 1.6R. A detailed calculation of the configurational entropy is

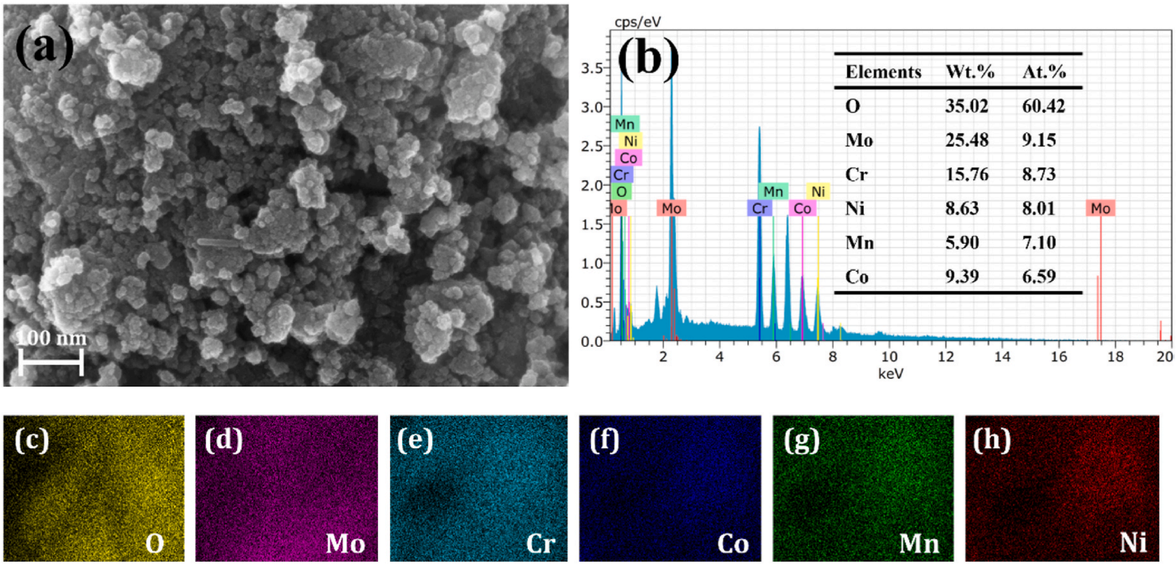

Elements	Wt.%	At.%
O	35.02	60.42
Mo	25.48	9.15
Cr	15.76	8.73
Ni	8.63	8.01
Mn	5.90	7.10
Co	9.39	6.59

Fig. 3. (a) FE-SEM image, (b) EDX pattern, and (c–h) Elemental mapping of HEO O15 nanoparticles.

provided in the supplementary data.

HR-TEM analysis has been conducted to further explore the morphology and microstructure of the HEO O15 nanoparticles. Fig. 4a and b depicts the TEM images of HEO O15 nanoparticles at different magnifications (100 and 50 nm), revealing a spherical morphology with agglomeration. The SAED pattern (Fig. 4c) of the HEO O15 nanoparticles shows well defined continuous rings with bright spots, indicating that the synthesized HEOs nanoparticles are polycrystalline in nature. The SAED pattern's four diffraction rings correspond to (111), (222), (400) and (440) planes, respectively. The particle size distribution of the HEO O15 nanoparticles was assessed from the TEM image using image J software, and the average particle size was found to be approximately 15 nm (Fig. 4d). Furthermore, a clear lattice fringes were observed in the HR-TEM images (Fig. 4e and f), indicating the higher crystallinity of material. The distance between adjacent lattice planes obtained are 0.25, 0.28, 0.207 and 0.49 nm, corresponding to (311), (220), (400) and (111) planes, respectively. The agreement between the SAED pattern, HR-TEM analysis, and XRD pattern indicates that the synthesized HEOs nanoparticles exhibit a single-phase spinel structure.

The surface area is regarded as a key element influencing electrocatalytic performance. N_2 adsorption/desorption isotherms have been performed to estimate the BET surface area, pore size and pore volume of the HEOs nanoparticles, as shown in Fig. S2. The adsorption/desorption isotherms resemble typical type IV isotherms. The obtained BET surface area, pore size and pore volume of the HEOs nanoparticles were depicted in Table 2. According to BET model, the HEO O15 exhibits the higher BET surface area of 86.4 m^2g^{-1} among other HEOs nanoparticles. The obtained results demonstrate that the BET surface area increases with increasing the oxygen vacancy. The existence of oxygen vacancies indicates the emergence of structural or surface imperfections, which tends to increasing the surface roughness and pore formation in the material. As a result, increasing surface roughness and pore formation provide more accessible surface area for gas adsorption, resulting in a larger BET surface area. Previous studies suggested that the electrocatalyst with large BET surface area would be a most efficient choice [32]. In this thermal plasma technique, high surface area HEO nanoparticles are produced, which improve the electron-electrolyte interaction and make them excellent for electrocatalytic activity.

Table 2
BET surface area, pore size and pore volume of the HEOs nanoparticles.

S. No	Sample	Surface area (m^2 g^{-1})	Pore size (nm)	Pore volume (cm^3g^{-1})
1	HEO O0	28.1	11.7	0.083
2	HEO O5	71.1	8.2	0.103
3	HEO O10	73.9	6.1	0.114
4	HEO O15	86.4	6.0	0.135

The surface chemistry and oxidation states of the HEOs nanoparticles were investigated using surface-sensitive XPS analysis. As depicted in Fig. 5, it confirms the presence of all the constituent elements (Ni, Co, Mn, Mo, Cr) in the as-synthesized (HEO O0) and Ar-plasma treated HEOs nanoparticles (HEO O5, HEO O10, and HEO O15). Moreover, the acquired XPS data revealed differences in the binding energy of all elements in the HEOs nanoparticles after Ar-plasma treatment. The Co 2p XPS spectrum (Fig. 5a) can be deconvoluted into four peaks. The peaks at 784.1 and 797.2 eV are attributed to Co^{2+} 2p3/2 and Co^{2+} 2p1/2, respectively, whereas the other two peaks are placed at 795.7 (Co^{3+} 2p1/2) and 781.2 eV (Co^{3+} 2p3/2). The peaks centered at 787.6 and 803.3 eV are the associated satellite peaks. The relative ratio of Co^{2+}/Co^{3+} was calculated by taking the area under the peak, which exhibits HEO O15 (1.01) have higher than that of HEO O0 (0.32), HEO O5 (0.52) and HEO O10 (0.69), respectively. The XPS spectra of Cr 2p are shown in Fig. 5b, with two peaks at 586.6 and 576.6 eV, corresponding to the spin-orbital coupling of Cr^{3+} 2p1/2 and Cr^{3+} 2p3/2, respectively, while the peaks of Cr^{4+} 2p1/2 and Cr^{4+} 2p3/2 are located at 588.6 and 578.06 eV. The Cr^{3+}/Cr^{4+} relative ratio of HEO O15 (1.6) was greater than HEO O0 (1.2), HEO O5 (1.29) and HEO O10 (1.33), which was well matched with the previously stated result [25].

As shown in Fig. 5c, two oxidation states of Mn 2p, that is, Mn^{2+} (641.8 eV) and Mn^{3+} (644.1 eV), were found in Mn $2p_{3/2}$, and the peaks

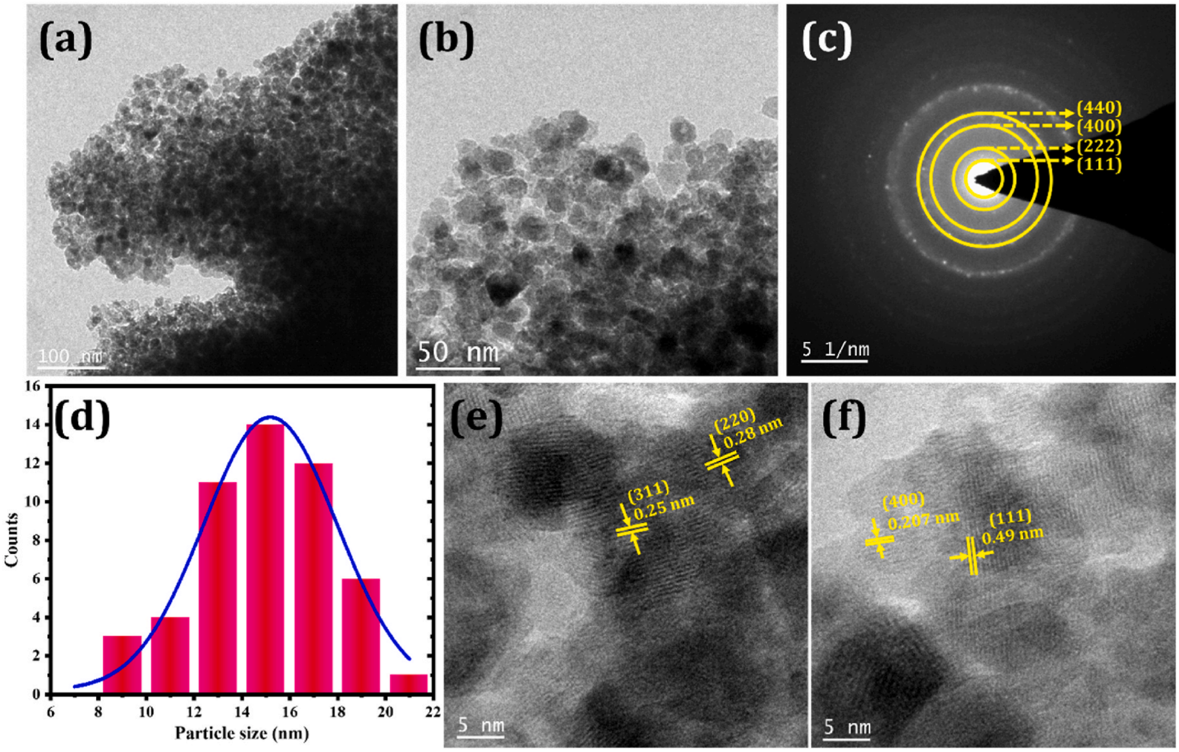

Fig. 4. (a & b) Low and high magnification TEM images, (c) SAED pattern, (d) Particle size distribution, and (e & f) HR-TEM images of HEO O15 nanoparticles.

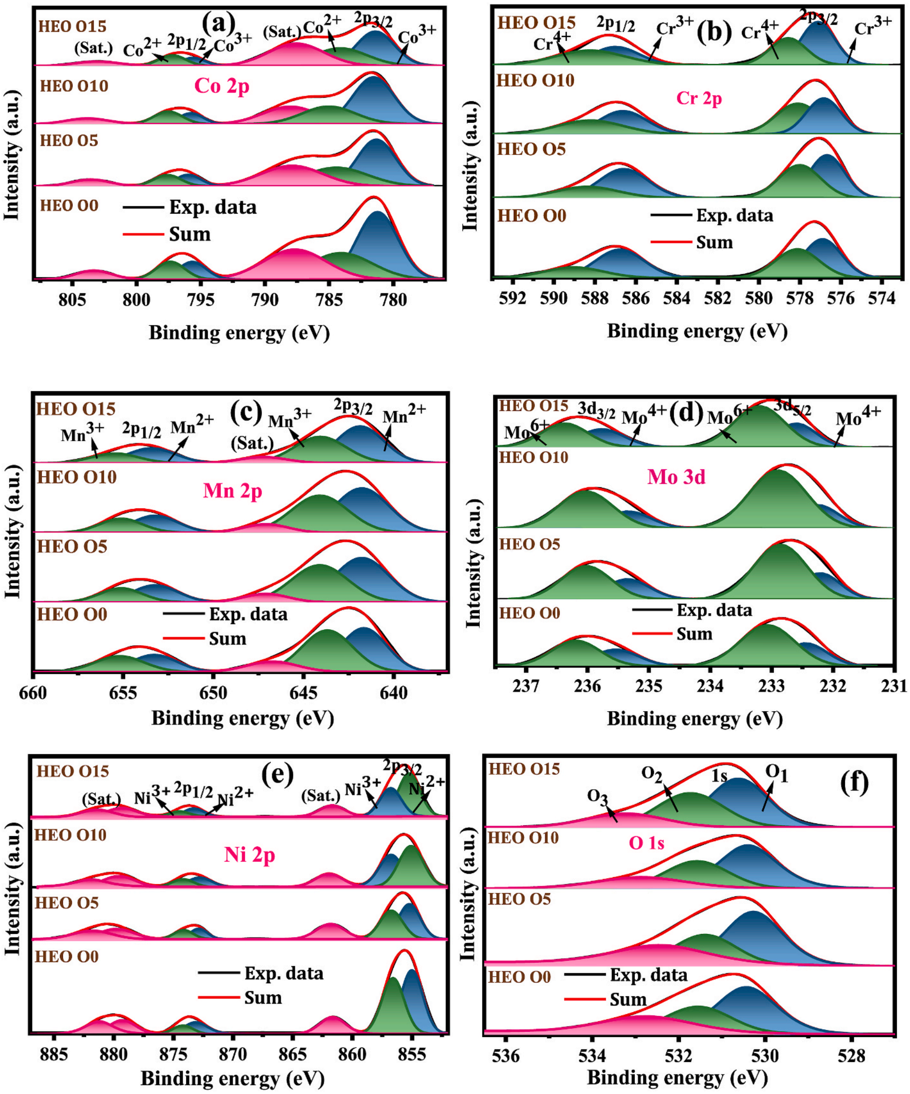

Fig. 5. XPS spectra of HEOs nanoparticles, (a) Co 2p, (b) Cr 2p, (c) Mn 2p, (d) Mo 3d, (e) Ni 2p, and (f) O 1s.

at 653.3 (Mn^{2+}) and 655.2 eV (Mn^{3+}) correspond to Mn $2p_{1/2}$. In addition, a satellite peak at 647.02 eV is ascribed to Mn $2p_{3/2}$. Herein, Mn^{2+}/Mn^{3+} relative ratio of HEO O0, HEO O5, HEO O10 and HEO O15 was found to be 1.02, 1.22, 1.36 and 1.39, respectively. The fine-scan Mo 3d XPS spectra (Fig. 5d) were deconvoluted into four fitted peaks with the spin-orbit characteristic of Mo^{4+} and Mo^{6+}. The peaks centered at 233.02 and 236.1 eV corresponds to Mo^{6+}, and the peaks located at 235.5 and 232.6 eV can be ascribed to Mo^{4+}. The Ni 2p XPS spectra (Fig. 5e) was deconvoluted into Ni^{2+}, Ni^{3+} and the satellite peak. The Ni 2p peaks at binding energies of 873.1 and 855.05 eV with a satellite signal at 881.4 and 879.1 eV were characteristic of Ni^{2+}. The peaks at 874.2 and 856.6 eV with the satellite signal at 861.9 eV belongs to Ni^{3+}. The HEO O15 (1.46) nanoparticles showed a greater Ni^{2+}/Ni^{3+} ratio than HEO O0 (1.1), HEO O5 (1.25), and HEO O10 (1.3) [32]. The O 1s spectra (Fig. 5f) was deconvoluted into three distinct peaks O_1, O_2 and O_3 located at 530.3, 531.5 and 533.1 eV, which were ascribed to lattice oxygen (M−O metal-oxygen bond), oxygen vacancies, and surface absorbed oxygen, respectively. Notably, the peak area of O_2 (oxygen vacancies) varied significantly between the four HEO nanoparticles, with the area of the peak increasing as the Ar-plasma treatment period increased. This observation clearly demonstrates the effect of plasma treatment time on the development of oxygen vacancies over the HEO surface. This is most likely due to metastable Ar ions transferring internal energy to the surface of HEOs nanoparticles, causing the loss of oxygen atoms from the lattice surface [33]. The formation of oxygen vacancies during plasma treatment can cause lattice distortions and electronic density changes, resulting in a minor shift of this peak towards higher or lower binding energies, depending on the degree of vacancy generation and charge redistribution. Consequently, oxygen vacancies can alter the electronic structure, create more electrochemically active sites and enhance the dynamics adsorption of adsorbates, thus significantly boosting the water splitting kinetics [34].

Since the presence of oxygen vacancies in the HEOs nanoparticles was firmly validated by XPS analysis, an additional EPR study was conducted to further assess the comprehensive information regarding the presence of oxygen vacancies in the HEOs nanoparticles. EPR spectroscopy can investigate unpaired electronic states in materials to validate the presence of defects, free radicals, etc., as well as qualitatively characterise the concentration of oxygen vacancies in materials [35]. All the HEOs nanoparticles exhibit EPR peak at magnetic field around 3510 G, as displayed in Fig. S3, which are caused by unpaired electrons trapped on the surface of oxygen vacancies, and they correspond to the EPR signal detected at $g = 2.004$ [36]. Herein, the intensity gradually increases with increasing the Ar-plasma treatment time, which illustrates the increase in oxygen vacancies. HEO O15 exhibits the highest intensity than the other three HEOs nanoparticles, indicating that it possesses more oxygen vacancies. The obtained EPR results are consistent with the XPS result.

The optical band gap of HEOs nanoparticle was estimated using diffuse reflectance spectroscopy (DRS). The Kubelka-Munk (K-M) plot was generated using the reflectance data by plotting $(F(R_\infty)*E)^n$ against the $h\nu$ and displayed in Fig. S4.

$$F(R_\infty)=\frac{\left((1-R_\infty)^2\right)}{2R_\infty} \tag{1}$$

$$F(R_\infty)E=\left(h\nu - E_g\right)^n \tag{2}$$

where R_∞ is the reflectance, E (=$h\nu$) is the energy, h is Planck's constant, ν is the cut-off frequency, E_g is the band gap, and the value of n is 1/2. The obtained band gap values are 2.92, 2.75, 2.62 and 2.5 eV for HEO O0, HEO O5, HEO O10 and HEO O15, respectively. When an oxygen atom is removed from the surface of a metal oxide, it creates an electron-rich environment, causing the fermi level to shift closer to the conduction band and the valence band to shift upward. Hence, the bandgap of HEO nanoparticles decreased with increasing the oxygen vacancy [37]. In this case, HEO O15 has a narrower bandgap than other HEOs nanoparticles, resulting in improved electronic conductivity. Consequently, the higher electrical conductivity promotes the charge transfer between the electrode and electrolyte interface, which is beneficial for the water splitting reaction [38].

3.2. *Electrocatalytic OER performance of HEOs in 1 M KOH electrolyte*

The as-synthesized and Ar-plasma treated HEOs are subjected to electrocatalytic oxygen evolution reaction in 1 M KOH solution using a conventional three-electrode set-up. The modified NF (nickel foam), Hg/HgO and Pt-ring has been utilized as working, reference and counter electrode. Initially, all the HEOs are activated by performing the cyclic voltammetry (CV) cycles at a high scan rate of 100 mV/s for 10 cycles. Further, a 5 mV/s CV was performed on HEOs to assess their catalytic activity using the backward scan (to eliminated the anodic oxidation peak around 1.3 V (*vs* RHE) which belongs Ni^{3+} from the NF) and the obtained LSVs are provided in Fig. 6a. The LSV polarization results with 60 % iR compensation demonstrates that HEO O15 showed superior OER performance by demanding a lesser overpotential of 246 mV to reach a current density of 50 mA cm^{-2}. The HEO O10, HEO O5, HEO O0 and bare NF showed inferior catalytic activity than the HEO O15 with an overpotential of 255, 263, 274 and 420 mV to reach the same current density, respectively. Furthermore, HEO O15 exhibits remarkably high catalytic activity, surpassing that of commercial RuO_2 (324 mV) with a high current density (600 mA cm^{-2}) essential for practical application. Furthermore, the radar plot in Fig. 6b, reinforces HEO O15's exceptional OER activity at high current densities (200 and 400 mA cm^{-2}) compared to other HEOs. Table S1 provides a comparison of the OER performance of HEO O15 with other recently reported HEO catalysts with similar characteristics. The electrochemical impedance spectroscopic (EIS) analysis was carried out to examine the resistance of all the HEOs. Fig. 6c demonstrates that HEO O15 exhibits less resistance towards electron transfer at the electrode-electrolyte interface with a (R_{ct}) charge transfer resistance value of 0.2 Ω. The other HEO O10, HEO O5 and HEO O0 showed high resistance compared to HEO O15 with a R_{ct} of 0.21, 0.224 and 0.23 Ω, respectively. The insight of Fig. 6c shows the corresponding equivalent circuit diagram utilized for fitting the EIS spectra [39]. Analysis of the Tafel slopes derived from the iR corrected LSV polarization outcomes in Fig. 6d reveals HEO O15's superior catalytic activity.

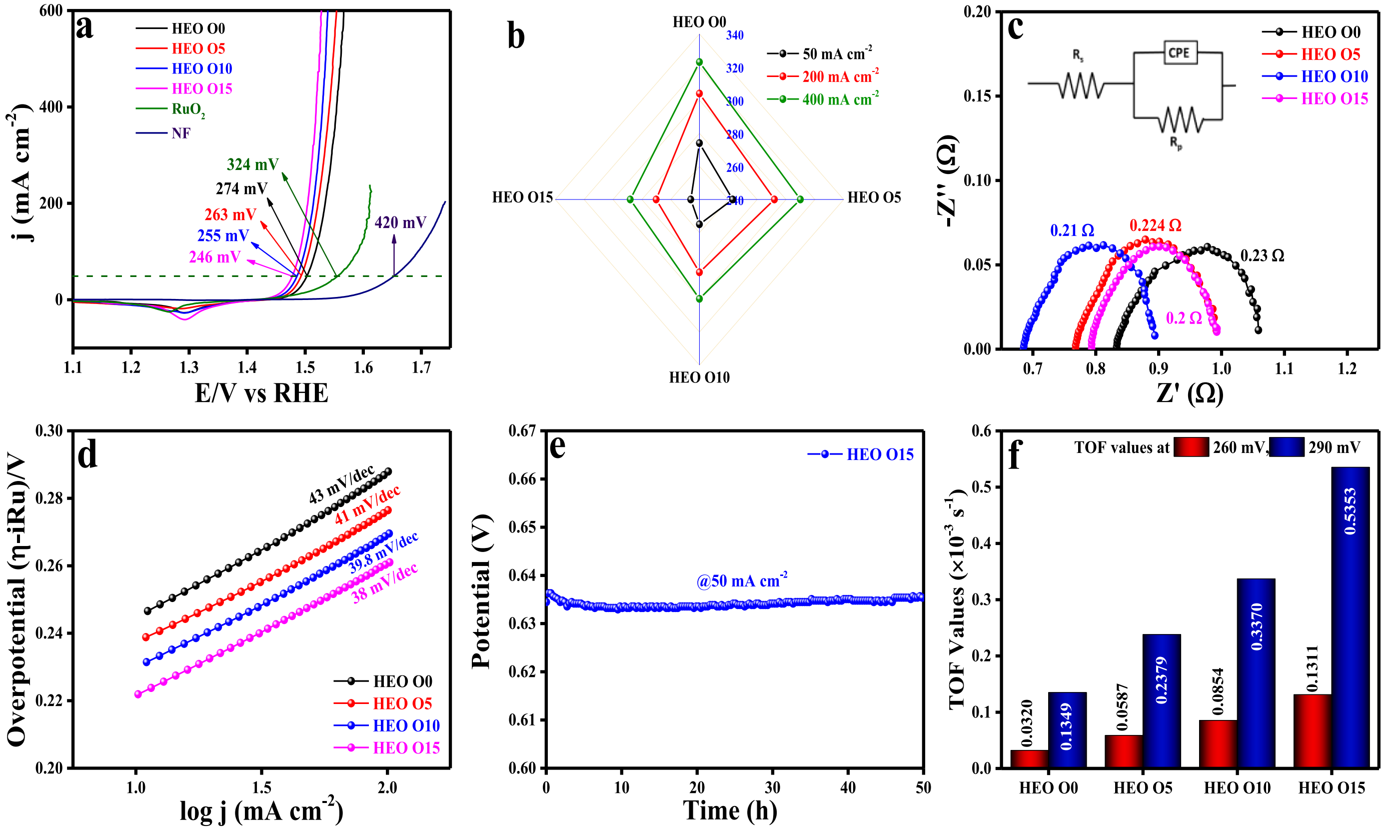

Fig. 6. Electrocatalytic OER performance: (a) The geometrically normalized LSV results for HEO O0, HEO O5, HEO O10, HEO O15, commercial RuO_2 and bare NF at 50 mA cm^{-2} current density, (b) The radar plot showed overpotential calculated at different current densities (50, 200 and 400 mA cm^{-2}), (c) Nyquist plot of HEO O0, HEO O5, HEO O10 and HEO O15 at 0.7 V (vs Hg/HgO), (d) Tafel slope values from the iR drop free LSV curves, (e) Chronopotentiometric analysis of HEO O15 at 50 mA cm^{-2} current density over 50 h, and (f) TOF values of HEO O0, HEO O5, HEO O10 and HEO O15 at 260 and 290 mV overpotential.

This is attributed to its faster electron transfer kinetics, evidenced by a significantly lower Tafel slope of 38 mV/dec compared to HEO O10 (39.8 mV/dec), HEO O5 (41 mV/dec), and HEO O0 (43 mV/dec). HEO O15 excelled in long-term stability, impressively maintaining its activity for 50 h at a current density of 50 mA cm^{-2} in 1 M KOH (Fig. 6e). This exceptional stability may make it a promising candidate for practical applications. In addition to investigating the geometric properties of the catalysts, their intrinsic activities were also evaluated. Turnover frequency (TOF) was evaluated to emphasize the amount of oxygen molecules liberated per active site per unit time. At two different overpotential 260 and 290 mV, the TOF has been assessed and portrayed as bar diagram in Fig. 6f. The TOF results showcases HEO O15 exhibits a TOF value of 0.1311 and 0.5353 $\times$ 10^{-3} s^{-1}, respectively which is obviously higher compared to HEO O10 (0.0854 and 0.3370 $\times$ 10^{-3} s^{-1}), HEO O5 (0.0587 and 0.2379 $\times$ 10^{-3} s^{-1}) and HEO O0 (0.0320 and 0.1349 $\times$ 10^{-3} s^{-1}). The electrochemically active surface area (ECSA) of the catalysts was determined by analyzing the double-layer capacitance (C_{dl}) derived from CV curves (Figs. S5a–d). These CVs were measured at various scan rates within a potential window of 0.1–0.3 V vs. Hg/HgO. Analysis of the CV curves yielded C_{dl} values of 0.0055, 0.005, 0.0047, and 0.0045 F for HEO O15, HEO O10, HEO O5, and HEO O0, respectively (Fig. S5e). These C_{dl} values were then used to calculate the electrochemically active surface area (ECSA) using the formula ECSA = C_{dl}/C_s, where C_s is the specific capacitance of a flat electrode surface, assumed to be 0.04 mF cm^{-2}. The evaluated ECSA values of HEO O15, HEO O10, HEO O5, and HEO O0 are 137.5, 125, 117.5 and 112.5 cm^2, respectively. The larger ECSA of HEO O15 underscores its advantage, indicating a greater number of exposed active sites accessible for the OER reaction. Notably, even after normalizing the LSV results based on ECSA (ECSA-normalized) (Fig. S6a), the activity trend remains consistent with the observed geometric activity trend. Further, normalizing the LSV results by catalyst mass (Fig. S6b) revealed a similar activity trend for all HEOs. The overpotentials required to achieve a current density of 50 mA cm^{-2} were 249, 256, 265, and 274 mV for HEO O15, HEO O10, HEO O5, and HEO O0, respectively.

To delve deeper into HEO O15's intrinsic activity, measurements at 1.524 V vs RHE portrayed in Fig. S6c unveiled a superior specific and mass activity of 3.64 mA cm^{-2} and 473.42 mA/mg, respectively with a loading of ~1.0 mg cm^{-2}. Further, to gain deeper insights into the electron transfer processes occurring at the electrode-electrolyte interface, *operando*-electrochemical impedance spectroscopy (EIS) was performed at various potentials for each HEOs (Figs. S7a–d). The resulting Nyquist plots offer a visualization of the distinct electrochemical behaviours of the different materials. Additionally, the Bode plots were analysed for all HEOs, and the corresponding results are presented in Figs. S8a–d. The Bode plots offer insights into the adsorption/desorption of OH^- on the electrode surface at different frequencies. The high-frequency (HF) region likely reflects the oxidation of the electrocatalyst (HEOs) itself, while the low-frequency (LF) region might reveal the non-uniform distribution of oxidizing species at the electrode interface. Furthermore, the plot of R_{ct} vs applied voltage in Fig. S7e suggests that between 1.37 V and 1.44 V (vs. RHE), oxidation of the electrocatalyst (HEOs) happened at the HF phase angle. At voltage exceeding and beyond 1.44 V (vs. RHE), a significant drop in the LF phase angle could be attributed to the initiation of the OER on the electrode surface. To analyse the EIS data, a simple electrical circuit model consisting of two resistors (R1 and R2) connected in series (Fig. S7f). This model represents the interplay between electron transfer (electrooxidation) and mass transport processes occurring at the electrode surface during the reaction. The EIS analysis suggests that HEO O15 exhibits lower interfacial resistance compared to other catalysts. This suggests faster electron transfer kinetics at the electrode-electrolyte interface, making HEO O15 a more efficient OER catalyst. To assess the dynamic stability of HEO O15, an accelerated degradation (AD) study was conducted. The catalyst underwent 1000 CV cycles at a high scan rate of 150 mV s^{-1}. Following the AD test, LSV polarization curves were recorded (Fig. S9a). These results showcase the remarkable stability of HEO O15. After 1000 CV cycles, the overpotential increased by only 8 mV, indicating minimal performance degradation. The EIS analysis (Fig. S9b) aligns well with the findings from the LSV measurements, further supporting the exceptional stability of HEO O15. While a slight decrease in OER activity is observed after the 1000 CV cycles, could be attributed to the gradual accumulation of charge on the electrode surface during the OER process. This charge accumulation might hinder the adsorption of OH^- ions, a one of the crucial steps in the reaction. The Faradaic efficiency (FE) of the most promising catalyst, HEO O15, was further confirmed using a rotating ring-disk electrode (RRDE) experiment (Fig. S10). This technique revealed an impressive efficiency of 95.15 % in an alkaline medium. During the experiment, oxygen bubbles produced at the disk electrode were efficiently captured and reduced by the surrounding Pt ring held at a constant potential of −0.3 V. This remarkable Faradaic efficiency highlights the high selectivity of HEO O15 towards the OER, signifying minimal side reactions and efficient conversion of O_2 molecules.

3.3. Electrocatalytic HER performance of HEOs in 1 M KOH electrolyte

Following the evaluation of their OER activity, all the HEO catalysts were further investigated for their ability to perform the HER in the same 1 M KOH electrolyte using a three-electrode system. After the activation of all the catalyst via CV cycling at high scan rate, a 5 mV/s LSV was recorded to evaluate the performance of the catalyst. The LSV polarization results with 60 % iR compensation of all the HEOs are depicted in Fig. 7a. As like OER, HEO O15 requires a low overpotential of only 197 mV to achieve a current density of 50 mA cm^{-2}, outperforming HEO O10 (210 mV), HEO O5 (225 mV), HEO O0 (235 mV), and NF (307 mV). Notably, the commercially available Pt/C catalyst exhibits even better HER activity, reaching the same current density at a very low overpotential of 130 mV. Further, analysis of EIS in Fig. 7b, showed that HEO O15 possess less resistance towards the transfer of electron at the electrode-electrolyte interface with a low R_{ct} of 0.68 Ω, than HEO O10 (1.19 Ω), HEO O5 (1.39 Ω) and HEO O0 (1.7 Ω). This efficient electron transfer is further corroborated by the Tafel slope analysis from the corrected LSV curves. HEO O15 displays the lowest Tafel slope (93 mV/dec), signifying faster reaction kinetics compared to the other HEO O10 (96 mV/dec), HEO O5 (101 mV/dec) and HEO O0 (109 mV/dec). These combined factors lower electron transfer resistance and faster reaction kinetics, contribute to HEO O15's superior HER performance. Additionally, the radar plot in Fig. 7d demonstrates that HEO O15 maintains superior performance at higher current densities (200 and 400 mA cm^{-2}). Further, the HER performance was compared with the previously reported similar type of HEOs as given Table S2. The chronopotentiometry test in Fig. 7e showcases the exceptional long-term durability of HEO O15. At a current density of 50 mA cm^{-2}, it exhibits stable operation for 47 h in 1 M KOH with minimal degradation in the applied potential compared to the initial value. To quantify the catalytic activity for HER, turnover frequencies (TOF) were calculated for all catalysts at overpotential of 220 mV and 260 mV. As illustrated in the bar graph of Fig. 7f, HEO O15 exhibits significantly higher TOF values (0.2291 and 0.5715 x 10^{-3} s^{-1}) compared to other HEOs (HEO O10 (0.1624 and 0.4094 $\times$ 10^{-3} s^{-1}), HEO O5 (0.1195 and 0.3094 $\times$ 10^{-3} s^{-1}) and HEO O0 (0.0861 and 0.2229 $\times$ 10^{-3} s^{-1})) at 220 and 260 mV overpotential, respectively. These higher TOF values indicate that HEO O15 has a greater capacity to generate hydrogen molecules per unit active site per unit time. These findings are further corroborated by the mass-normalized LSV curves in Fig. S11a. The overpotential required to achieve a specific current density again follow the trend: HEO O15 (199 mV) < HEO O10 (214 mV) < HEO O5 (226 mV) < HEO O0 (236 mV). Additionally, HEO O15 demonstrates a remarkable mass activity of 318.4 mA/mg at 0.275 V vs. RHE, highlighting its superior performance even when considering catalyst mass (Fig. S11b). Further, HEO O15's dynamic stability was assessed by performing CV for 500 cycles at a high

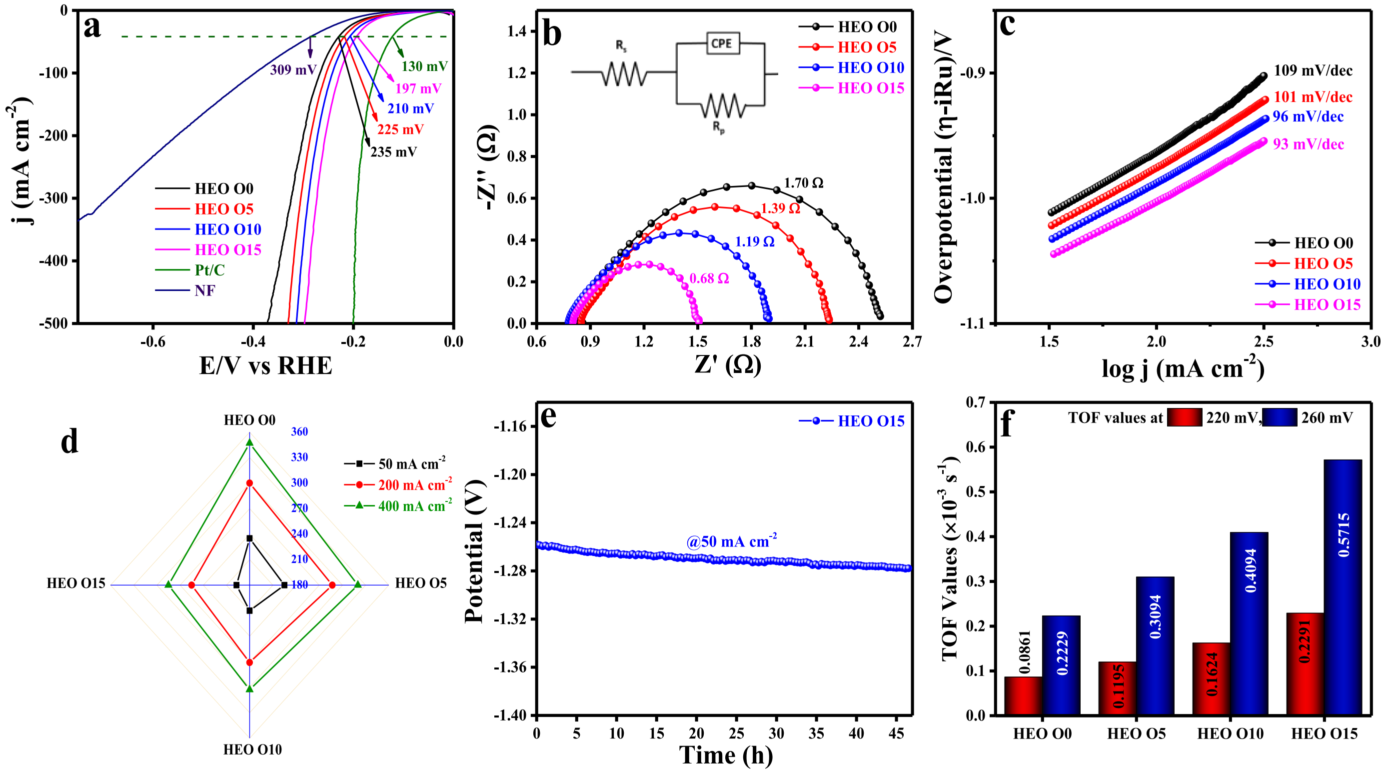

Fig. 7. Electrocatalytic HER performance: (a) The geometrically normalized LSV results for HEO O0, HEO O5, HEO O10, HEO O15, commercial Pt/C and bare NF at 50 mA cm^{-2} current density, (b) Nyquist plot of HEO O0, HEO O5, HEO O10 and HEO O15 at −1.25 V (vs Hg/HgO), (c) Tafel slope values from the iR drop free LSV curves, (d) The radar plot showed overpotential calculated at different current densities (50, 200 and 400 mA cm^{-2}), (e) Chronopotentiometric analysis of HEO O15 at 50 mA cm^{-2} current density over 47 h, and (f) TOF values of HEO O0, HEO O5, HEO O10 and HEO O15 at 220 and 260 mV overpotential.

scan rate of 100 mV/s. The LSV polarization curves (Fig. S12a) recorded after this CV cycling showed only a marginal increase in overpotential of 10 mV compared to the initial HEO O15, indicating minimal performance degradation. This finding aligns well with the EIS analysis results in Fig. S12b, further supporting the exceptional stability of HEO O15.

3.4. Electrocatalytic overall water splitting performance of HEO O15 in 1 M KOH electrolyte

Based on the impressive OER and HER performance of HEO O15 in 1 M KOH, a two-electrode configuration was employed for overall water splitting. Notably, HEO O15 functioned as both the cathode and anode (HEO O15 || HEO O15) and achieved a remarkable cell voltage of 1.58 V to deliver a current density of 10 mA cm^{-2}. The corresponding LSV results are presented in Fig. 8a. Furthermore, a long-term stability test (chronopotentiometry analysis) at a current density of 10 mA cm^{-2} showcased the exceptional stability of HEO O15 || HEO O15 for 65 h in 1 M KOH, as demonstrated in Fig. 8b. Table S3 compares the cell voltage achieved by HEO O15 || HEO O15 for overall water splitting with previously reported electrocatalysts.

To acquire a greater understanding of catalyst stability, HEO O15 underwent XPS analysis after the stability studies. The obtained result ensures that all the constituent materials are present in the HEO O15 after the stability test. Figs. S13a–f depicts the XPS spectra of Ni, Co, Mn, Cr, Mo and O of HEO O15 before and after OER and HER cycling investigations. The obtained XPS results illustrate that, compared to all elements, Mn and Co metal leashed out vigorously towards the electrolyte throughout the reaction, providing a higher surface area for OH$^-$ adsorption. Meantime, the XPS spectra of Cr 2p, Mo 3d, and Ni 2p peaks shifting towards lower binding energies confirms that these metal

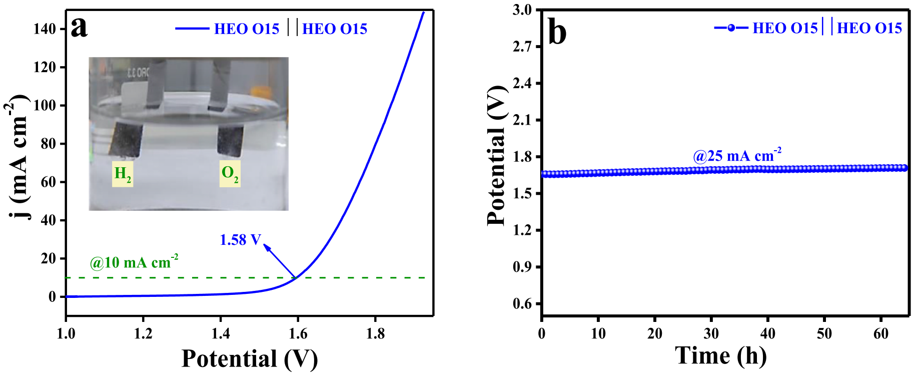

Fig. 8. (a) LSV polarization curves of HEO O15 || HEO O15 toward overall water splitting, and (b) Long-term durability test of HEO O15 || HEO O15 for overall water splitting at an applied current density of 10 mA cm^{-2} for 65 h in 1 M KOH solution.

cations may play a direct or indirect role in the OER and HER processes. During electrochemical OER and HER reactions, the surface charge density changes corresponding to the applied potential. These changes can primarily influence the electronic environment of surface atoms, results in shifts of binding energy towards the lower energy level. The direction of shift in the binding energy was depending on the nature of the charge redistribution rather than the specific OER or HER reactions [40]. Concurrently, oxygen vacancy emerged dramatically after the electrochemical stability test. During electrochemical reactions, oxygen ions on the metal surface are removed, resulting in a large number of oxygen vacancies on the surface. In addition to boosting H_2O adsorption, oxygen vacancy lowers the electrocatalyst's (HEO O15) charge transfer resistance and increases its surface reactive sites. After the electrochemical stability investigations, the electrocatalyst's morphology was further examined using FE-SEM analysis and the outcomes are displayed in Figure S14 (a-d). The obtained FE-SEM images revealed a significant morphological change that occurred throughout the electrochemical process. After 1000 CV cycles of OER reaction, the spherical morphology was reconstructed into nano flakes, whereas, after 500 CV cycles of HER reaction, the spherical morphology of the electrocatalyst was converted into nano needle-like structure. Fig. S15 depicts the elemental mapping of HEO O15 after OER and HER reactions after CV cycles. The obtained results showcase that all the constituent metals were homogeneously distributed in the HEOs nanoparticles, ensuring that all that metal cations remained in the HEOs electrodes after stability test.

4. Conclusion

This study efficiently produced HEOs $(Ni, Co, Cr, Mn, Mo)_3O_4$ nanoparticles using a DC non-transferred arc thermal plasma reactor. Low pressure Ar-glow discharge plasma treatment was adopted to create oxygen vacancies over the HEOs surface systematically. The oxygen vacancy rises proportionally with the period of Ar-plasma exposure, affecting the surface area and electronic structure of HEOs nanoparticles. The electrocatalytic activity of HEOs for OER and HER processes was primarily influenced by their surface area, oxygen vacancy, and the synergistic effect of the five metal cations. The oxygen vacancy-induced HEOs nanoparticles (HEO O15) demonstrate outstanding OER and HER activity, requiring a low overpotential of 246 and 197 mV to achieve a current density of 50 mA cm^{-2}. Based on the excellent OER and HER performance of HEO O15 led to the fabrication of two-electrode device with HEO O15 ∥ HEO O15 and it serves as both an anode and cathode. It demonstrates extraordinary activity at a low potential of 1.58 V to reach a current density of 10 mA cm^{-2} and has an exceptional long-term stability of 65 h. Obtained results suggest that plasma-assisted generation of oxygen vacancies on metal oxide surfaces is a promising strategy for enhancing the performance of HEOs-based functional materials in electrochemical water splitting reactions.

CRediT authorship contribution statement

Amarnath Pasupathi: Writing – original draft, Methodology, Investigation, Formal analysis, Data curation, Conceptualization. **Ragunath Madhu:** Writing – original draft, Resources, Investigation, Data curation. **Subrata Kundu:** Writing – review & editing, Validation, Resources, Investigation. **Yugeswaran Subramaniam:** Writing – review & editing, Supervision, Methodology, Funding acquisition.

Declaration of competing interest

The authors declare that they have no known competing financial interests or personal relationships that could have appeared to influence the work reported in this paper.

Acknowledgement

The authors thank the Central Instrumentation Facilities (CIF), Pondicherry University for characterization support. The authors would like to acknowledge DST-FIST level-II, at the Department of Physics, Pondicherry University for XRD analysis. R. M. wishes to acknowledge the Department of Science and Technology (DST) Inspire fellowship (SRF).

Appendix A. Supplementary data

Supplementary data to this article can be found online at https://doi.org/10.1016/j.jpowsour.2024.236144.

Data availability

Data will be made available on request.

References

[1] K.K. Joshi, P.M. Pataniya, G. Bhadu, C.K. Sumesh, Monometallic, bimetallic, and trimetallic chalcogenide-based electrodes for electrocatalytic hydrogen evolution reaction, Int. J. Hydrogen Energy 48 (2023) 7260–7272.
[2] A. Pasupathi, Y. Subramaniam, R. Murugan, A.P. V, J. Mostaghimi, L. Pershin, C. Batiot-Dupeyrat, Y. Kobayashi, Efficient dry reforming of methane through graphite cathode thermal plasma torch: impact of gas injection position, Fuel 371 (2024) 131954.
[3] P. Chawdhury, D. Ray, T. Vinodkumar, C. Subrahmanyam, Catalytic DBD plasma approach for methane partial oxidation to methanol under ambient conditions, Catal. Today 337 (2019) 117–125.
[4] X. Fang, X. Zhang, Y. Guo, M. Chen, W. Liu, X. Xu, H. Peng, Z. Gao, X. Wang, C. Li, Highly active and stable Ni/Y2Zr2O7 catalysts for methane steam reforming: on the nature and effective preparation method of the pyrochlore support, Int. J. Hydrogen Energy 41 (2016) 11141–11153, https://doi.org/10.1016/j.ijhydene.2016.04.038.
[5] S. Anantharaj, S. Noda, Amorphous catalysts and electrochemical water splitting: an untold story of harmony, Small 16 (2020) 1905779.
[6] R. Madhu, S.S. Sankar, K. Karthick, A. Karmakar, S. Kumaravel, S. Kundu, Electrospun cobalt-incorporated MOF-5 microfibers as a promising electrocatalyst for OER in alkaline media, Inorg. Chem. 60 (2021) 9899–9911.
[7] P. Amarnath, R. Madhu, K. Praveen, S. Govindarajan, S. Kundu, Y. Subramaniam, Phase-pure high-entropy spinel oxide (Ni,Fe,Mn,Cu,Zn)3O4 via thermal plasma: a promising electrocatalyst for oxygen evolution reaction, ACS Appl. Energy Mater. 6 (2023) 5899–5911.
[8] S. Kumaravel, K. Karthick, S.S. Sankar, A. Karmakar, R. Madhu, K. Bera, S. Kundu, Current progressions in transition metal based hydroxides as bi-functional catalysts towards electrocatalytic total water splitting, Sustain. Energy Fuels 5 (2021) 6215–6268.
[9] S.G. Peera, R. Koutavarapu, L. Chao, L. Singh, G. Murugadoss, G. Rajeshkhanna, 2D MXene nanomaterials as electrocatalysts for hydrogen evolution reaction (HER): a review, Micromachines 13 (2022) 1499.
[10] H.K. Sadhanala, V.K. Harika, T.R. Penki, D. Aurbach, A. Gedanken, Ultrafine Ruthenium oxide nanoparticles supported on molybdenum oxide nanosheets as highly efficient electrocatalyst for hydrogen evolution in acidic medium, ChemCatChem 11 (2019) 1495–1502, https://doi.org/10.1002/cctc.201801990.
[11] J.S. Kim, B. Kim, H. Kim, K. Kang, Recent progress on multimetal oxide catalysts for the oxygen evolution reaction, Adv. Energy Mater. 8 (2018) 1702774.
[12] A. Pasupathi, M. Perumal, E. Narayanamoorthi, B. Palanisamy, Y. Subramaniam, Electrochemical charge storage performance of (Mn, Ni, Mo, Co, Fe)3O4 high entropy oxide nanoparticles produced via thermal plasma route, Ceram. Int. 50 (15) (2024) 26740–26749.
[13] T. Li, Y. Yao, B.H. Ko, Z. Huang, Q. Dong, J. Gao, W. Chen, J. Li, S. Li, X. Wang, R. Shahbazian-Yassar, F. Jiao, L. Hu, Carbon-supported high-entropy oxide nanoparticles as stable electrocatalysts for oxygen reduction reactions, Adv. Funct. Mater. 31 (2021) 2010561.
[14] K.H. Tian, C.Q. Duan, Q. Ma, X.L. Li, Z.Y. Wang, H.Y. Sun, S.H. Luo, D. Wang, Y. G. Liu, High-entropy chemistry stabilizing spinel oxide (CoNiZnXMnLi)3O4 (X = Fe, Cr) for high-performance anode of Li-ion batteries, Rare Met. 41 (2022) 1265–1275.
[15] K. Xiaolin, Iwase, honma, high-entropy spinel oxide nanoparticles synthesized via supercritical hydrothermal processing as oxygen evolution electrocatalysts, J. Mater. Chem. A 5 (2022) 9292–9296.
[16] B. Talluri, K. Yoo, J. Kim, High entropy spinel metal oxide (CoCrFeMnNi)3O4 nanoparticles as novel efficient electrocatalyst for methanol oxidation and oxygen evolution reactions, J. Environ. Chem. Eng. 10 (2022) 106932.
[17] C. Duan, X. Li, D. Wang, Z. Wang, H. Sun, R. Zheng, Y. Liu, Nanosized high entropy spinel oxide (FeCoNiCrMn)3O4 as a highly active and ultra-stable electrocatalyst for the oxygen evolution reaction, Sustain. Energy Fuels 6 (2022) 1479–1488.

[18] P. Amarnath, N. Nandy, B. Indumathy, S. Yugeswaran, Study on CO2 based thermal plasma torch and its effective utilization for material processing in atmospheric pressure, J. CO2 Util. 66 (2022) 102290.

[19] A. P, Y. S, S. K, N.P. K, Influence of transferred arc plasma melting time on the formation of phase and microstructure of mullite-zirconia composite, Front. Adv. Mater. Res. (2021) 34–42.

[20] D. Stenzel, B. Zhou, C. Okafor, M.V. Kante, L. Lin, G. Melinte, T. Bergfeldt, M. Botros, H. Hahn, B. Breitung, S. Schweidler, High-entropy spinel-structure oxides as oxygen evolution reaction electrocatalyst, Front. Energy Res. 10 (2022) 1–11.

[21] C.F. Chen, G. King, R.M. Dickerson, P.A. Papin, S. Gupta, W.R. Kellogg, G. Wu, Oxygen-deficient BaTiO3-x perovskite as an efficient bifunctional oxygen electrocatalyst, Nano Energy 13 (2015) 423–432.

[22] Y. Wang, T. Zhou, K. Jiang, P. Da, Z. Peng, J. Tang, B. Kong, W. Bin Cai, Z. Yang, G. Zheng, Reduced mesoporous Co3O4 nanowires as efficient water oxidation electrocatalysts and supercapacitor electrodes, Adv. Energy Mater. 4 (2014) 1–7.

[23] C. Meng, M. Lin, X. Sun, X. Chen, X. Chen, X. Du, Y. Zhou, Laser synthesis of oxygen vacancy-modified CoOOH for highly efficient oxygen evolution, Chem. Commun. 55 (2019) 2904–2907.

[24] D. Zhou, X. Xiong, Z. Cai, N. Han, Y. Jia, Q. Xie, X. Duan, T. Xie, X. Zheng, X. Sun, X. Duan, Flame-engraved nickel–iron layered double hydroxide nanosheets for boosting oxygen evolution reactivity, Small Methods 2 (2018) 1–7.

[25] S. Ding, Y. Sun, F. Lou, L. Yu, B. Xia, J. Duan, Y. Zhang, S. Chen, Plasma-regulated two-dimensional high entropy oxide arrays for synergistic hydrogen evolution: from theoretical prediction to electrocatalytic applications, J. Power Sources 520 (2022).

[26] A. Pasupathi, Y. Subramaniam, A novel strategy for rapid synthesis of nanostructured high-entropy metal oxides through thermal plasma for supercapacitor applications, Energy Fuels 38 (6) (2024) 5534–5544.

[27] Y. Vadikkeettil, P. Amarnath, S. Yugeswaran, P.V. Ananthapadmanabhan, Comparative study of plasma torch characteristics using air and carbon dioxide, IEEE Trans. Plasma Sci. 50 (2022) 1395–1400.

[28] Q. Wen, Y. Li, C. He, M. Shen, F. Ning, X. Dan, Y. Liu, P. Xu, S. Zou, Z. Chai, W. Li, L. He, B. Tian, X. Zhou, A recyclable standalone microporous layer with interpenetrating network for sustainable fuel cells, Adv. Mater. 35 (2023) 2301504.

[29] Z. Li, X. Zhou, S. Singh, X. Wei, C. Guo, W. Li, Degradation of platinum electrocatalysts for methanol oxidation by lead contamination, Chin. Chem. Lett. 34 (2023) 2022–2024.

[30] C. Zhu, C. Li, M. Zheng, J.J. Delaunay, Plasma-induced oxygen vacancies in ultrathin hematite nanoflakes promoting photoelectrochemical water oxidation, ACS Appl. Mater. Interfaces 7 (2015) 22355–22363.

[31] K. Lakshmanan, A. Pasupathi, B. Narayanan, Y. Subramaniam, S. Gurusamy, Plasma assisted single-step synthesis of carbon-coated SrFe2O4 electrodes for enhancing supercapacitor and oxygen evolution reaction, Surface. Interfac. 55 (2024) 105339.

[32] A. Pasupathi, R. Madhu, S. Kundu, Y. Subramaniam, Effect of carbon infusion on water splitting performance of (Ni0.2 Co0.2 Cr0.2 Mn0.2 V0.2)3O4 high entropy oxides nanoparticle synthesized via thermal plasma, Electrochim. Acta 497 (2024) 144621.

[33] H. Han, S. Jin, S. Park, Y. Kim, D. Jang, M.H. Seo, W.B. Kim, Plasma-induced oxygen vacancies in amorphous MnOx boost catalytic performance for electrochemical CO2 reduction, Nano Energy 79 (2021) 105492.

[34] M. R, S.K. Karmakar, Karthick Kannimuhtu Arun, Oxygen Vacancy Enriched NiMoO4 Nanorods via Microwave Heating: a Promising Highly Stable Electrocatalyst for Total Water Splitting _ Enhanced Reader.Pdf, vol. 9, 2021 11691.

[35] S. Yang, Y. Liu, Y. Hao, X. Yang, W.A. Goddard, X.L. Zhang, B. Cao, Oxygen-vacancy abundant ultrafine Co3O4/graphene composites for high-rate supercapacitor electrodes, Adv. Sci. 5 (2018), https://doi.org/10.1002/advs.201700659.

[36] N.S. Gultom, Y.C. Zhou, D.H. Kuo, A facile and efficient method for preparing La-doped Co3O4 by electrodeposition as an efficient air cathode in rechargeable zinc-air batteries: role of oxygen vacancies, J. Colloid Interface Sci. 655 (2024) 394–406, https://doi.org/10.1016/j.jcis.2023.11.021.

[37] M.M. El-Nahass, H.S. Soliman, A. El-Denglawey, Absorption edge shift, optical conductivity, and energy loss function of nano thermal-evaporated N-type anatase TiO2 films, Appl. Phys. Mater. Sci. Process 122 (2016) 1–10, https://doi.org/10.1007/s00339-016-0302-6.

[38] M.M. Hassan, W. Khan, A. Azam, A.H. Naqvi, Effect of size reduction on structural and optical properties of ZnO matrix due to successive doping of Fe ions, J. Lumin. 145 (2014) 160–166, https://doi.org/10.1016/j.jlumin.2013.06.024.

[39] Y. Liu, B. Tian, F. Ning, Y. Li, C. Zhao, C. He, Q. Wen, X. Dan, Z. Chai, W. Li, M. Shen, L. He, W. Li, X. Zhou, Hybrid 3D-ordered membrane electrode assembly (MEA) with highly stable structure, enlarged interface, and ultralow Ir loading by doping nano TiO2 nanoparticles for water electrolyzer, Adv. Energy Mater. 14 (2024) 2303353.

[40] Q. Qin, L. Chen, T. Wei, X. Liu, MoS2/NiS yolk–shell microsphere-based electrodes for overall water splitting and asymmetric supercapacitor, Small 15 (2019) 1–13.